






# Sea surface warming patterns drive hydrological sensitivity uncertainties

Received: 17 May 2022

Accepted: 20 April 2023

Published online: 25 May 2023

 Check for updatesShipeng Zhang <sup>1</sup>✉, Philip Stier <sup>1</sup>, Guy Dagan <sup>2</sup>, Chen Zhou <sup>3</sup> & Minghuai Wang <sup>3</sup>

The increase in global-mean precipitation with global-mean temperature (hydrological sensitivity;  $\eta$ ) is constrained by the atmospheric energy budget, but its magnitude remains uncertain. Here we apply warming patch experiments to a climate model to demonstrate that the spatial pattern of sea surface warming can explain a wide range of  $\eta$ . Warming in tropical strongly ascending regions produces  $\eta$  values even larger than suggested by the Clausius–Clapeyron relationship ( $7\% \text{ K}^{-1}$ ), as the warming and moisture increases can propagate vertically and be transported globally through atmospheric dynamics. Differences in warming patterns are as important as different treatments of atmospheric physics in determining the spread of  $\eta$  in climate models. By accounting for the pattern effect, the global-mean precipitation over the past decades can be well reconstructed in terms of both magnitude and variability, indicating the vital role of the pattern effect in estimating future intensification of the hydrological cycle.

It is an essential but challenging goal to improve the projection of precipitation change under global warming<sup>1–3</sup>. The Clausius–Clapeyron relationship provides a strong constraint on increasing water vapour content per unit temperature warming (at around  $7\% \text{ K}^{-1}$ ), but it does not apply to the global-mean precipitation change, which is constrained by the atmospheric energy budget<sup>4,5</sup>. The latent heat released from precipitation has to be balanced by the atmospheric radiative cooling (ARC) and the surface sensible heat flux in equilibrium. Increasing greenhouse emissions will initially reduce global-mean rainfall<sup>4,6</sup>, corresponding to the decreased ARC when the surface temperature remains unchanged (that is, a rapid adjustment). For longer timescales, after the surface subsequently gets warmer, the ARC is enhanced, allowing for an intensification of the hydrological cycle<sup>7,8</sup>.

The change in temperature-mediated global-mean precipitation ( $P$ ) is suggested to be proportional to surface temperature ( $T$ ) increase<sup>4,9,10</sup>, and the ratio is referred to as hydrological sensitivity ( $\eta$ ), defined as follows:

$$\eta = \frac{\delta P/P}{\delta T} \text{ (in } \% \text{ K}^{-1}\text{)}. \quad (1)$$

$\eta$  is a widely used metric for evaluating intensification of the hydrological cycle. Compared to apparent hydrological sensitivity, which also takes into account rapid adjustments, the spread of  $\eta$  has been largely reduced and has been estimated to be around  $2\% \text{ K}^{-1}$  (ref. 2,4,9), predominately determined by the increased rate of radiative cooling from a deepening troposphere<sup>11</sup>. However, there remains a large inter-model spread in current global climate models (GCMs)<sup>2</sup>, even with identical configuration for numerical experiments<sup>10,12</sup>.

Under a relatively uniform global warming, the slower rate of increase in global-mean precipitation than the rate of increase in water vapour can lead to a slow-down of global circulation<sup>7,13,14</sup> and prolonged water vapour lifetime<sup>15</sup>, which directly affects regional and seasonal rainfall intensity and frequency<sup>16,17</sup> with important social impacts. Robust responses in regional atmospheric dynamic systems (and the associated rainfall) are more relevant to the evolving patterns of warming<sup>14,18–22</sup>, despite their large model dependence<sup>23–25</sup>. However, the sea surface temperature (SST) warming pattern effects on global-mean precipitation and further on  $\eta$  are less noticed, because changes in global-mean precipitation are suggested to be dominated by the thermodynamics and energetic budget<sup>4,26,27</sup>.

<sup>1</sup>Atmospheric, Oceanic and Planetary Physics, Department of Physics, University of Oxford, Oxford, UK. <sup>2</sup>Fredy and Nadine Herrmann Institute of Earth Sciences, The Hebrew University of Jerusalem, Jerusalem, Israel. <sup>3</sup>Joint International Research Laboratory of Atmospheric and Earth System Sciences and School of Atmospheric Sciences, Nanjing University, Nanjing, China. ✉e-mail: [shipeng.zhang@physics.ox.ac.uk](mailto:shipeng.zhang@physics.ox.ac.uk)

Previous studies on  $\eta$  have typically focused on global-mean temperature changes without considering surface warming patterns. However, the pattern effect resulting from non-uniform SST warming has recently been shown to be important for clouds feedbacks<sup>28–30</sup>, as well as radiative feedback parameters more generally<sup>31,32</sup>. Given that these terms can also affect the atmospheric energy budget<sup>5,33</sup>, it is reasonable to expect that SST warming patterns also play a role in hydrological cycle intensification. Considering that the SST pattern was and will be changing due to the internal variability of the climate system<sup>34,35</sup> and that spatially inhomogeneous warming is to be expected under the global warming scenario<sup>13,31,36</sup>, it is therefore of interest to investigate the dependence of  $\eta$  on SST warming patterns.

To examine this, we start with analysing  $\eta$  estimated from an ensemble of simulations with Community Atmospheric Model 5 (CAM5)<sup>37,38</sup> forced with 80 SST warming and cooling patches individually placed across the globe (Fig. 1a). Only experiments with statistically different changes in surface temperature are analysed (Methods).

## Dependence of hydrological sensitivity on regional warming

Previously,  $\eta$  has been treated as a time-independent parameter in each model, reflecting its distinct atmospheric physics parameterizations<sup>2,10,39</sup>. However, Fig. 1 indicates that the spatial pattern of SST warming has a remarkable impact on the magnitude of  $\eta$ . Different warming patch locations superposed on the climatological SST pattern in CAM5 generate a wide range of  $\eta$  (Fig. 1b). Interestingly, the peak (2.2% K<sup>-1</sup>) of the estimated probability density function of  $\eta$  falls within the likely range of  $\eta$  (approximately 1% K<sup>-1</sup> to 3.5% K<sup>-1</sup>) estimated by tens of GCMs<sup>2,12,40</sup>. This means that by changing only the spatial warming pattern, one model can reproduce an even wider spread of  $\eta$  than estimated by tens of GCMs. Furthermore, the value of  $\eta$  estimated from abrupt4xCO<sub>2</sub> experiment (a quadrupling of CO<sub>2</sub> concentration simulation; a commonly used experiment to estimate  $\eta$  under global warming<sup>12</sup>) using the same atmospheric model is also shown as reference ( $\eta = 2.7\% \text{ K}^{-1}$ , blue dashed line in Fig. 1b). Notably, larger  $\eta$  values are associated with warming patches located in lower latitudes, especially in regions with strong climatological ascent (solid red dots in Fig. 1a).

Investigations into different patch experiments confirm the general latitude dependence of  $\eta$  and its variability (Supplementary Fig. 1), which can be traced back to the dependence of global-mean precipitation and temperature on localized SST warming (Extended Data Fig. 1). By using the Green's function approach (Methods), we find that both global-mean precipitation (Fig. 1c) and temperature responses (Fig. 1d) are more sensitive to warming in the tropical west Pacific and Atlantic Oceans, where the localized increase in SST can remotely warm the tropical free troposphere due to the intense convection and strong circulation<sup>30,38</sup>. After dividing the global precipitation response (Fig. 1c) by the near-surface temperature anomaly (Fig. 1d), we obtain the dependence of  $\eta$  on localized SST changes (Fig. 1e). The model tends to predict large  $\eta$  in response to warming in regions of strong large-scale ascent (Supplementary Fig. 3), such as the Indo-west-Pacific tropical ocean and tropical Atlantic (Fig. 1e). More interestingly, some experiments even predict  $\eta$  larger than the water vapour increase rate at 7% K<sup>-1</sup> (Fig. 1b,e), that is a super-Clausius–Clapeyron rate. These high values are robust and cannot be simply explained by the small global-mean temperature changes (Fig. 1d and Supplementary Fig. 4).

Why is the magnitude of  $\eta$  more sensitive (sometimes even at super-Clausius–Clapeyron rate) to warming in strong tropical ascent regions? One explanation can be traced to the robust response of atmospheric circulation to inhomogeneous warming. The water cycle can be approximated as a process carrying water vapour from the boundary layer to the free troposphere through ascending motion and associated condensation, with precipitation of a large fraction of the water<sup>7</sup>. In global mean, this process can be written as  $P = M_c q$  (ref. 7),

where  $M_c$  is the convective mass flux, and  $q$  refers to the typical boundary layer mixing ratio. The relative changes in precipitation can be written as  $\delta P/P = \delta M_c/M_c + \delta q/q$  and be understood theoretically from changes in its thermodynamical (that is,  $\delta q/q$ ; due to changes in atmospheric moisture content) and dynamical (that is,  $\delta M_c/M_c$ ; due to changes in circulations) components. Changes in  $q$  closely follow the Clausius–Clapeyron scaling at around 7% K<sup>-1</sup> (ref. 25,41) (Supplementary Fig. 5), with slight deviations due to the responses over lands<sup>42</sup>. Therefore,  $\delta P/P = \delta M_c/M_c + 0.07\delta T$  can be used to diagnose the relationship between the response of global convective mass flux (and circulation) and precipitation<sup>7,13,43</sup>. That is, a weakened ( $\Delta M_c/M_c < 0$ ) or strengthened ( $\Delta M_c/M_c > 0$ ) circulation can lead to  $\eta$  being smaller or greater than 7% K<sup>-1</sup>, respectively.

Although  $M_c$  is not directly available in CAM5 output, changes in large-scale upward vertical pressure velocity at 500 hPa ( $\Delta\omega_{500}^+$ ) serves as a good metric of global circulation changes and are well correlated with changes in  $M_c$  (ref. 13). Figure 1f shows that localized warming in strong ascending regions can lead to stronger upward motions and an acceleration of the circulation ( $\Delta M_c/M_c > 0$ ), resulting in a super-Clausius–Clapeyron  $\eta$  (red dots in Fig. 1f). In contrast, warming patches in experiments with  $\eta$  lower than the average ( $\eta < 2\% \text{ K}^{-1}$ ; blue dots in Fig. 1f) are mostly located in regions of strong descent (that is, the descending branch of the Walker and Hadley circulations), indicating a substantially slowed-down circulation. Figure 1e,f have a spatial correlation of  $-0.33$ , which is statistically significant ( $P$  values below 0.01), evidencing the underlying link between  $\eta$  and circulation changes.

Figure 2 illustrates the large-scale circulation response to SST warming patch locations. The strong ascent at the warm pool serves as a water vapour ‘pump’ to transport boundary layer water vapour to the free troposphere (Fig. 2a). Warming in warm pool strengthens the circulation and increases convective mass flux (Fig. 2b), while warming in subsidence branches weakens the circulation and decreases convective mass flux (Fig. 2c) (details in Supplementary Text 1). Being the ascending centre of both Walker and Hadley circulations, combined with the positive feedback between convection and circulation<sup>23,44</sup>, makes the tropical west Pacific Ocean critical in driving global circulation and transporting water vapour to the free troposphere. It is also noteworthy that the perturbation is not limited to SST; strong absorbing aerosols have recently been shown to have the ability to alter the circulation and then the effective radiative forcing as well<sup>45</sup>.

Alternatively, the variability of  $\eta$  in the patch experiments can also be understood using the framework in ref. 23. Combining equation (3) in ref. 23 and equation (1) in this work,  $\eta$  can be approximated as

$$\eta = \frac{\delta P}{P\delta T} \approx \frac{\overline{\alpha P_{\text{local}} \delta T^*}}{P\delta T} + \beta, \quad (2)$$

where  $T^*$  is the deviation of local temperature from global mean,  $P_{\text{local}}$  is the local precipitation, the overbar notation indicates a spatially weighted averaging over the globe, and  $\alpha$  and  $\beta$  are two positive constants measuring the local precipitation response to  $T^*$  and global-mean temperature increase, respectively. The second term on the right-hand side refers to the hydrological responses under uniform warming, and the first term measures the hydrological responses to the deviation from uniform warming. When there is a warming in tropical ascent regions,  $P_{\text{local}} > P$  for regions with  $\delta T^* > 0$ , so the first term on the right-hand side of equation (2) is positive, and  $\eta > \beta$ ; if the warming locates in tropical subsidence regions,  $P_{\text{local}} < P$  for regions with  $\delta T^* > 0$ , and  $P_{\text{local}} > P$  for regions with  $\delta T^* < 0$ , so  $\eta < \beta$ . Therefore,  $\eta$  tends to be large for patch experiments with warming in the tropical ascent regions.

The dependence of global-mean precipitation on SST warming patterns is also consistent with the atmospheric energy budget framework, which involves a balance between global-mean latent heat released from precipitation, ARC and surface sensible heat flux<sup>5,46</sup>. The

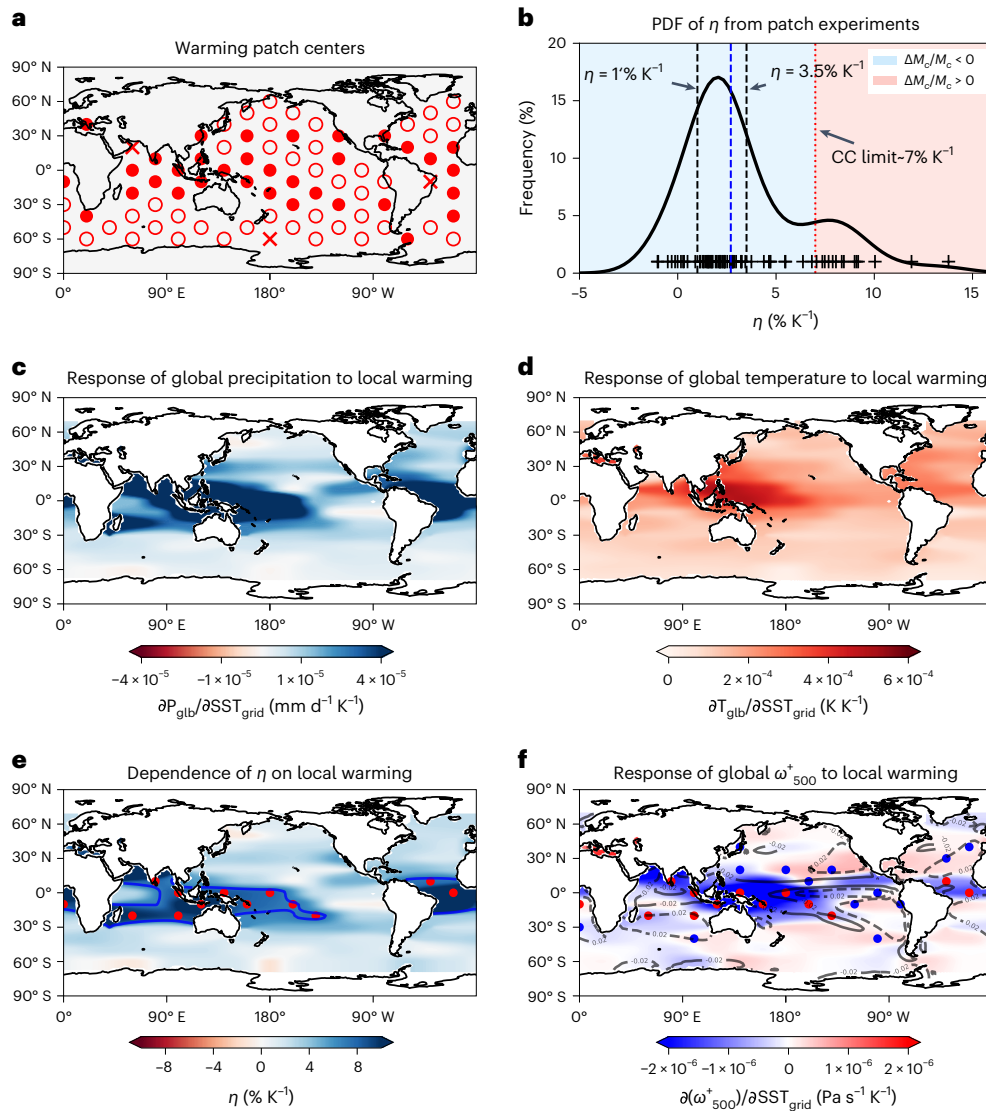


**Fig. 1 | SST warming patch experiments.** **a**, The geographical location of warming patches centre. Red solid dots indicate the patch experiments that show larger hydrological sensitivity ( $\eta$ ) than the one estimated from the abrupt4xCO<sub>2</sub> experiment (blue dashed line in **b**) using the same atmospheric model, whereas red circles indicate the patch experiments with smaller  $\eta$ , and red crosses indicate the experiments with no statistically significant changes in global-mean temperature. **b**, The estimated probability density function (PDF) of  $\eta$  derived from patch experiments that show significantly different ( $P$  values below 0.01) global-mean surface temperature to baseline experiment. Each plus sign indicates the hydrological sensitivity estimated from the corresponding patch experiment. Vertical dashed black lines denote the approximate upper and lower bounds of  $\eta$  estimated from current GCMs, respectively, whereas the vertical dashed red line denotes the water vapour increase rate suggested by the

Clausius–Clapeyron (CC) relation. The blue area indicates a decrease in convective mass flux ( $\Delta M_c/M_c < 0$ ) and a slowed-down circulation, whereas the red area denotes an increase in convective mass flux ( $\Delta M_c/M_c > 0$ ) and a speed-up circulation. **c–f**, Dependence of global-mean precipitation (**c**), temperature (**d**),  $\eta$  (**e**), and upward vertical pressure velocity at 500 hPa ( $\omega_{500}^+$ ) with amplitude larger than 0.05 hPa s<sup>-1</sup> (**f**) to SST changes in each grid box. The blue contour line in **e** indicates the rate of 7% K<sup>-1</sup>. Red dots in **e** and **f** indicate the patch experiments that show  $\eta$  larger than 7% K<sup>-1</sup>, whereas blue dots in **f** indicate the ones that show  $\eta$  smaller than 2% K<sup>-1</sup>. Blue colours in **f** indicate enhanced upward motion, and red colours indicate otherwise. Contour lines in **f** refer to the baseline vertical pressure velocity at 500 hPa, with solid lines for upward motions and dashed lines for downward motions.

responses from ARC account for most of the  $\eta$  spread (Supplementary Fig. 6) and resemble the global precipitation response distribution (Supplementary Fig. 7). Both clear-sky and cloudy-sky responses contribute to the ARC changes<sup>33,47</sup> (Fig. 3a,b). For clear sky, warming in tropical ascent regions is amplified at free tropospheric levels (that is the lapse rate feedback) and actively propagated to remote regions, increasing temperature globally (the Planck effect) and the associated column-integrated water vapour amount (Fig. 3c), leading to increased clear-sky ARC and eventually enhanced precipitation. In contrast, warming in the subtropics and tropical descent regions remains localized, resulting in smaller changes globally (Fig. 3a). For cloudy sky,

warming in extratropical and tropical descent regions is confined to local scales, reducing local low cloud amounts and cloudy-sky ARC due to a decrease in local tropospheric stability. However, warming in tropical ascent regions can be communicated to remote regions via moist adiabatic processes, resulting in globally increased tropospheric stability, non-local low cloud amounts (Supplementary Figs. 8 and 9) and cloudy-sky ARC (Fig. 3b) (more details in Supplementary Fig. 10 and Supplementary Text 2).

Both the qualitative large-scale circulation perspective and the quantitative energy budget perspective suggest that warming in the tropical ascent region leads to an ‘invigorated’ response of circulation

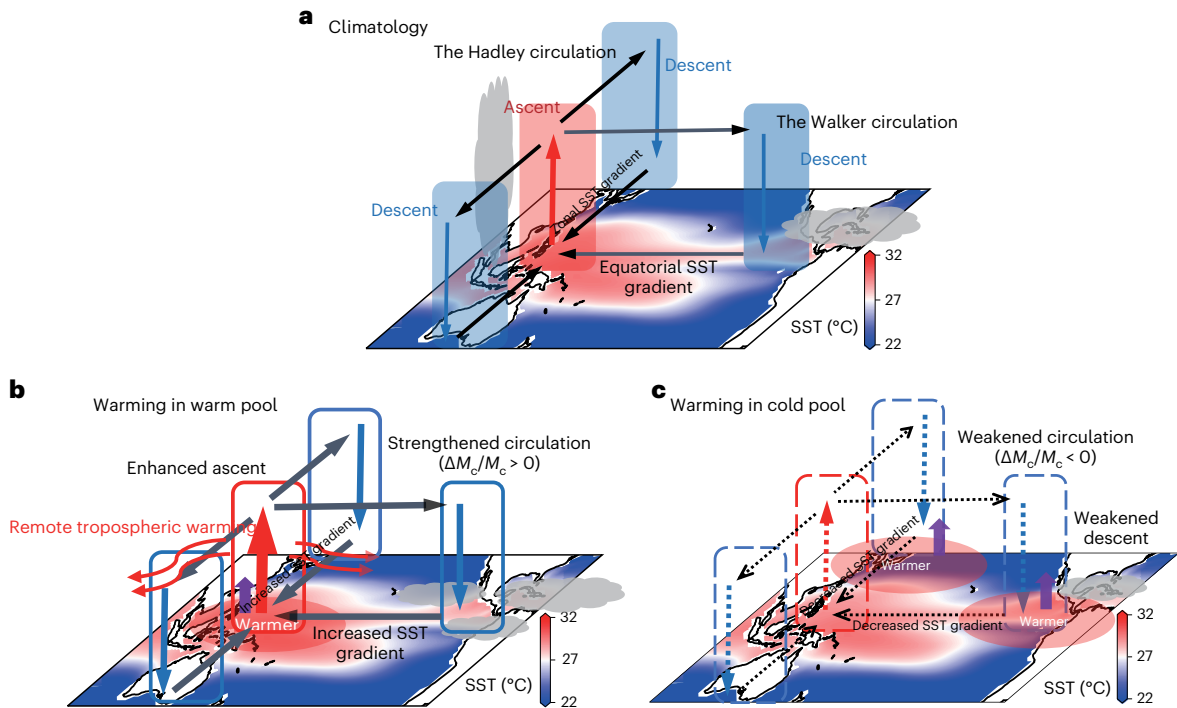


**Fig. 2 | Schematic illustration of the large-scale circulation response to different SST warming patch locations.** **a**, A conceptual representation of the climatological Hadley and Walker circulation. The western equatorial Pacific is dominated by strong large-scale ascent due to the warm surface, while the subtropics (Hadley circulation) and eastern equatorial Pacific (Walker circulation) are dominated by prevailing descent as the subsidence branch. **b**, Warming patches superposed on the warm pool induce anomalous ascent and increase the zonal and equatorial SST gradient, leading to a strengthening of the large-scale circulation. This is indicated by a stronger global-mean ascent at

500 hPa ( $\Delta\omega_{500}^+ < 0$ ) and increased convective mass flux ( $\Delta M_c/M_c > 0$ ). Besides, this warming can also be communicated to the remote free troposphere and increase inversion strength, leading to an increased global low-cloud cover. **c**, Warming patches superposed on the subsidence branch regions induce anomalous ascent, reducing the prevailing descent which opposes the Hadley and Walker circulation. Together with the decreased zonal and equatorial SST gradient, it weakens the circulation, leading to weakened global-mean ascent ( $\Delta\omega_{500}^+ > 0$ ) and decreased convective mass flux ( $\Delta M_c/M_c < 0$ ). The background figure in **a–c** is the SST climatology in the CAM5 model.

and ARC (Fig. 2b), whereas warming in the descent region leads to a ‘dampened’ response (Fig. 2c), which results in a bimodal distribution of  $\eta$  (Fig. 1b and Extended Data Fig. 2).

### Estimates of the pattern effect across GCMs

Given that SST patterns can evolve differently in fully coupled models even for identical forcing<sup>48,49</sup>, the spread of  $\eta$  among GCMs can therefore arise from: (1) different global-mean precipitation responses to a given warming pattern and (2) different SST warming patterns per degree global-mean warming (under the same external forcing). The calculation of  $\eta$  based on equation (1) can then be expanded as follows:

$$\eta = \frac{\partial P/P}{\partial \text{SST}(\text{pattern})} \times \frac{\partial \text{SST}(\text{pattern})}{\partial T}. \quad (3)$$

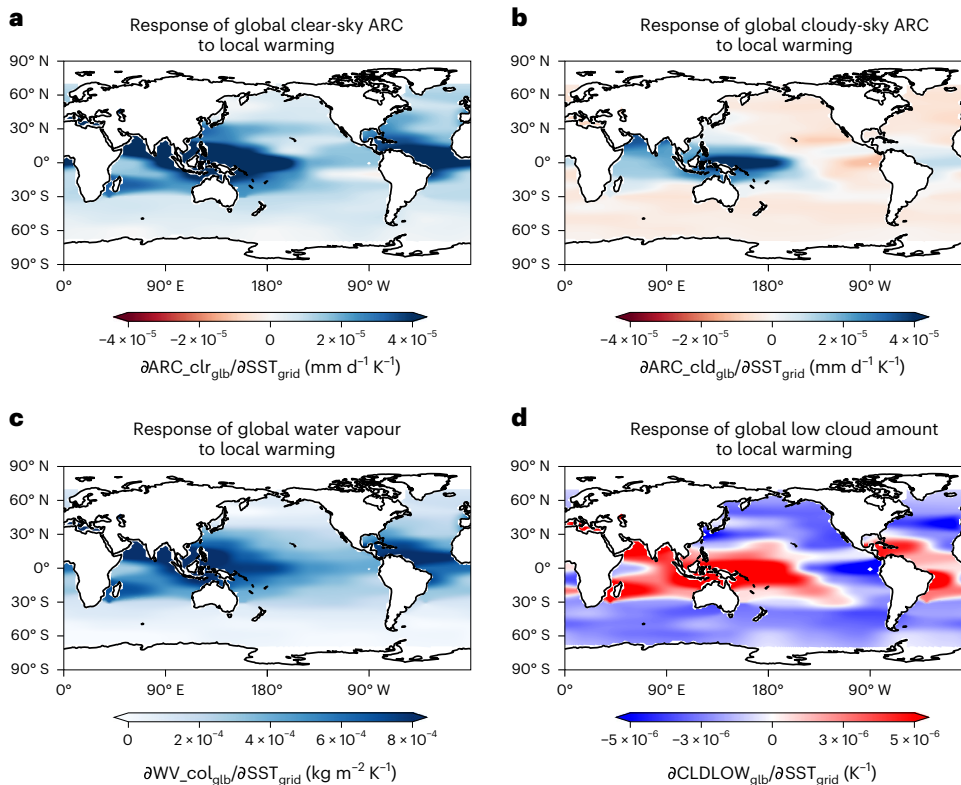
In this framework, the right hand-side consists of two terms. The first term reflects the atmospheric model differences, such as different parameterizations in water vapour shortwave absorption efficiency<sup>2</sup> and low cloud schemes<sup>50</sup>, in estimating precipitation responses to a certain warming pattern, hereafter denoted the atmospheric model term. The second term accounts for the variability of different SST warming patterns, hereafter denoted the pattern effect term.

In this Article, we investigate the spread of both terms across 24 fully coupled CMIP5 (Coupled Model Intercomparison Project Phase 5) models for the abrupt4xCO<sub>2</sub> experiments (Methods). Previous work studying the spread of  $\eta$  have primarily focused on the atmospheric model term<sup>2,10,50</sup>. However, Fig. 4 shows that the contribution from different SST warming patterns is equally important. The variation of

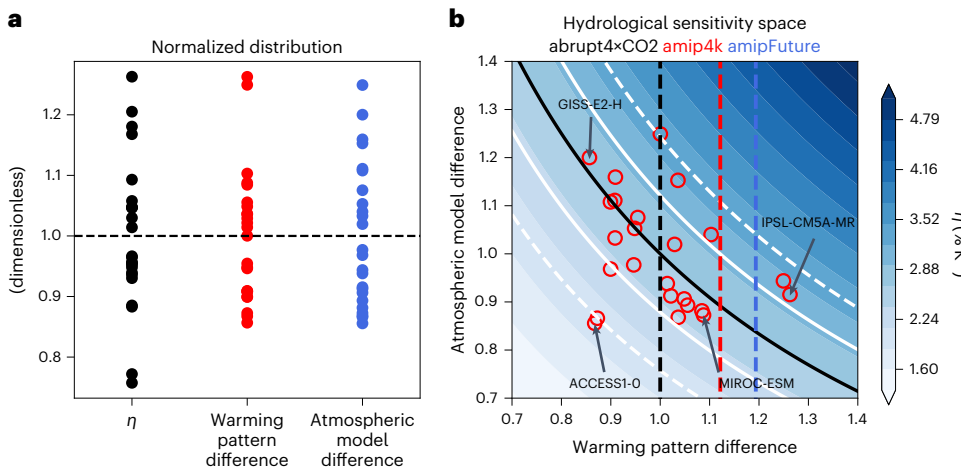
the warming pattern effect is as large as the atmospheric model difference and the spread of  $\eta$  (Fig. 4a). Even after removing the two outlier models (the IPSL-CM5A-MR and IPSL-CM5A-LR models) for warming pattern uncertainty (although their warming patterns are not unrealistic or too dramatic; Supplementary Fig. 12), the normalized warming pattern uncertainty has been narrowed down to about two thirds of the atmospheric model uncertainty, which is still not neglectable.

Figure 4b further shows the values of  $\eta$  from 24 CMIP5 coupled models in reconstructed  $\eta$  space (blue colours), which is determined by both the pattern effect and atmospheric model difference based on equation (3). This decomposition helps to distinguish the contributions to the large difference in  $\eta$  among models resulting from differences in atmospheric models or warming patterns. For instance, IPSL-CM5A-MR, the model with the largest pattern effect, has much more warming concentrated in the tropics (Supplementary Fig. 12) compared with the ACCESS1-0 model, which has the smallest pattern effect, leading to a larger  $\eta$  from IPSL-CM5A-MR, which supports our proposed mechanisms and strengthens our conclusions.

Some studies also use non-coupled atmosphere-only models with perturbed SST to study the precipitation responses<sup>12,39,51</sup>. Values of  $\eta$  estimated from amipFuture experiment (prescribed SST with global-mean 4 K but patterned SST increase) are systematically larger than those from amip4K experiment (prescribed SST with uniformly 4 K increase compared with present-day SST), which are then larger than those from the fully coupled abrupt4xCO<sub>2</sub> experiments (Extended Data Fig. 3). Differences in warming patterns may explain this discrepancy. A comparison of warming patterns from each experiment (vertical lines in Fig. 4b) shows that SST warming in amipFuture is more pronounced



**Fig. 3 | Geographical attribution of global responses to local SST changes.** **a–d**, Dependence of global-mean clear-sky ARC (**a**), cloudy-sky ARC (**b**), column-integrated water vapour (**c**) and low cloud amount (**d**) on SST changes in each grid box. All energetics are shown in equivalent precipitation units of millimetres per day.



**Fig. 4 | Attribution of hydrological sensitivity uncertainties in CMIP5 models.** **a**, Values of hydrological sensitivity ( $\eta$ ), warming pattern term and atmospheric model difference term from equation (3) for 24 CMIP5 models for the abrupt4xCO<sub>2</sub> experiment, normalized by the multi-model mean. **b**, Contribution of the normalized pattern effect and atmospheric model differences to the hydrological sensitivity space. Blue colours denote the  $\eta$  space estimated based on equation (3). Red circles denote the 24 CMIP5 models (Supplementary Table 1).

The solid black line, white solid lines and white dashed lines refer to the ensemble mean, one inter-model standard deviation and two inter-model standard deviations of the values of  $\eta$ , respectively. The vertical black dashed line, red dashed line and blue dashed line indicate the ensemble mean of pattern effect (normalized based on abrupt4xCO<sub>2</sub> ensemble mean) estimated from the abrupt4xCO<sub>2</sub>, amip4K and amipFuture experiments, respectively (Methods).

at low latitudes than in amip4K, while warming in amip4K is more pronounced at low latitudes than in abrupt4xCO<sub>2</sub> (Extended Data Fig. 4). More discussions can be found in Supplementary Text 3. This suggests that future work needs to consider variations in SST warming patterns when using different experiment set-ups to investigate the intensification of the hydrological cycle.

### Observational evidence

Properly accounting for the warming pattern effect is important not only for predicting future hydrological cycle state but also for understanding past changes. Figure 5a shows that the reconstructed precipitation (Methods), which considers the pattern effect based on Hadley Centre/Climatic Research Unit Temperature (HadCRUT) observed SST

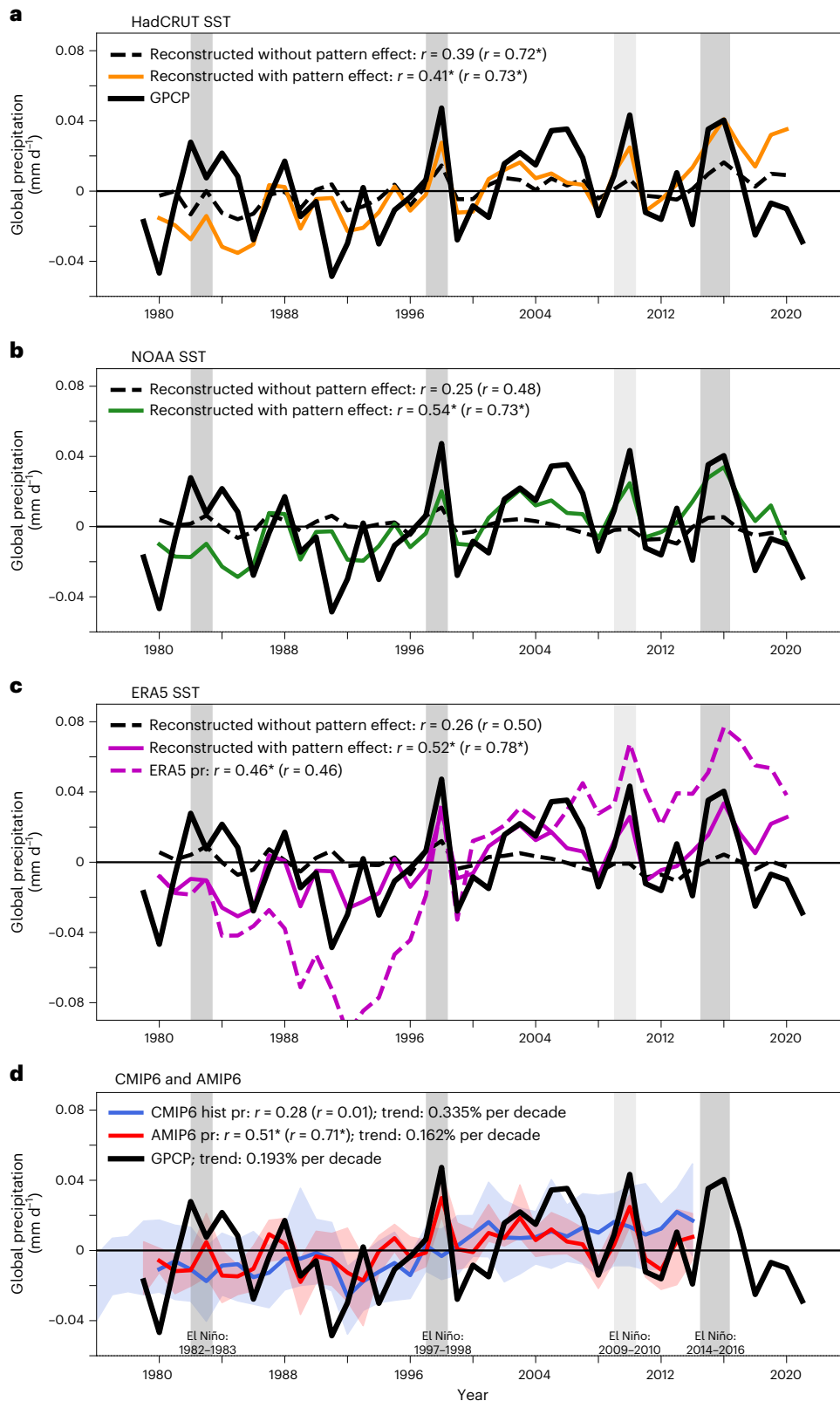


**Fig. 5 | Observed and reconstructed annual- and global-mean precipitation during 1980–2020. a**, Time series of observed precipitation anomaly from GPCP (solid black line), reconstructed precipitation anomaly without pattern effect (black dashed line; based on equation (19) in Methods) and reconstructed with pattern effect (orange line; based on equation (20) in Methods) based on HadCRUT observed SST datasets. **b**, Same as **a** but for reconstructed precipitation based on NOAA observed SST datasets. **c**, Same as **a** but for reconstructed precipitation based on SST from ERA reanalysis. The solid red line denotes the global-mean precipitation anomaly from ERA reanalysis.

**d**, Simulated global-mean historical precipitation (hist pr) from CMIP6 (blue line) and AMIP6 (red line) historical simulation ensemble mean with shading representing the inter-modal range. Dark grey shading indicates very extreme El Niño events (1982–1983, 1997–1998 and 2014–2016), and light grey indicates strong El Niño events (2009–2010).  $r$  denotes the correlation coefficient between reconstructed or simulated precipitation and GPCP observed precipitation, and the asterisk mark indicates the correlation is statistically significant (at 95% confidence level).  $r$  in brackets refers to the correlation coefficient after year 1995 when the GPCP dataset is suggested to be more reliable.

data, well reproduces the observed precipitation, whereas a reconstruction without the pattern effect does not. This is reflected in the improved correlation coefficient between observed and reconstructed precipitation, particularly after 1995 when the Global Precipitation Climatology Project (GPCP) dataset is deemed more reliable<sup>52</sup>. The slow component (mediated by surface temperature changes) accounting for the pattern effect can explain much of the interannual variability (Supplementary Fig. 15). Our conclusions remain robust when replacing the HadCRUT observed SST datasets with the US National Oceanic and Atmospheric Administration (NOAA) observed SST (Fig. 5b) and the fifth generation European Center for Medium-range Weather Forecasts (ECMWF) global reanalysis (ERA5) SST datasets (Fig. 5c), although some discrepancies may persist due to the different spatial and temporal sampling and calibrations used in the datasets<sup>53,54</sup>. The reconstructed precipitation based on ERA5 patterned SST dataset performs even better than ERA5 precipitation dataset (Fig. 5c), even though this approach is relatively simple. Moreover, during strong El Niño events, the observed and reconstructed (with the pattern effect) global-mean precipitation show larger magnitude of changes than the reconstructed one without the pattern effect (Fig. 5). This is consistent with previous studies suggesting that El Niño strongly enhances the Hadley circulation<sup>55,56</sup> as a result of tropical-mean warming and increased meridional SST gradient.

The implication of pattern effects on CMIP models can be seen by comparing CMIP6 and Atmospheric Model Intercomparison Project Phase 6 (AMIP6) historical simulations (Fig. 5d). Both sets of simulations use the same external forcing fields. The key difference is that SST is free to evolve in CMIP6 historical simulations, whereas it is prescribed from observations in AMIP6-hist simulations (Method). AMIP6-hist simulated precipitation captures observed inter-annual variability more accurately than CMIP6 historical simulations (Fig. 5d), despite the fact that global-mean SST in CMIP6 historical simulations reasonably resembles the observed SST (Supplementary Fig. 16). This indicates that the observed SST patterns are not reproduced in CMIP6 historical simulations, affecting their ability to simulate the global-mean precipitation variability. Thus, it is essential to accurately simulate not only the global mean but also the patterns of SST to better simulate global-mean precipitation. Observed and AMIP6 simulated global-mean precipitation show almost no trend over time, largely due to the suppressed global warming during 1998–2013 which resulted from a La-Niña-like Pacific cooling<sup>35</sup>. This cooling pattern weakened the water vapour<sup>37</sup> and precipitation response. However, CMIP6 historical simulations did not capture this La-Niña-like Pacific cooling pattern<sup>35,57</sup>, resulting in a stronger precipitation trend (Fig. 5d).

## Discussion

Our work shows that the warming pattern plays a crucial role in determining the magnitude of hydrological sensitivity ( $\eta$ ), which can therefore be time dependent, climate forcer dependent, model dependent and experiment dependent (prescribed SST or fully coupled set-up) via the warming pattern effect, rather than being constant for each model<sup>2,39</sup>. Moreover, previous work estimates the temperature-mediated precipitation responses using only global-mean temperature responses and neglects the important role of spatial SST patterns. Accounting for the pattern effect remarkably improves the reconstructed global-mean precipitation variations compared with observations, suggesting the temperature-mediated component of precipitation change can be caused by the variation of SST patterns, sometimes even in the absence of changes in global-mean temperature. Accounting for the pattern effect will help to reduce uncertainties in estimates of hydrological cycle intensification under global warming<sup>10,58,59</sup>.

If the warming occurs in regions with strong ascent, it could accelerate the circulation, enhance the transport of water vapour from the boundary layer to the free troposphere, increase ARC and potentially lead to a super-Clausius-Clapeyron  $\eta$ . It is, however, noteworthy that the distribution

of  $\eta$  shown in Fig. 1 may depend on the experiment design (such as patch size and magnitude of temperature increase) and the model used. Furthermore, this idealized patch-like warming is not likely to be sustained in the real world or a coupled model due to interactive responses between the wind, evaporation, ocean dynamics and thermocline<sup>21</sup>. Under real-world global warming scenarios, most warming is happening at higher latitudes, and the tropical SST remains nearly unchanged<sup>13</sup>. Besides, the SST pattern change can also lead to circulation shifts instead of altering their magnitude, which can be model dependent<sup>60</sup>.

Caution is recommended when relying on short-term historical observations of SST patterns to estimate the plausible range of the pattern effect. The warming pattern is evolving over time<sup>61</sup> as a result of coupled ocean–atmosphere processes<sup>21,62</sup>, meaning that a past trend cannot imply a future trend. In addition, different types and concentration of climate agents can lead to distinct SST warming (or cooling) patterns<sup>63,64</sup>, which adds extra uncertainties that rely on future emission scenarios. Moreover, short-term SST patterns are largely dependent on interannual variability, such as ENSO-related changes<sup>65</sup>. For example, estimates of  $\eta$  based on short-term observation (from 3.2% K<sup>-1</sup> (ref. 25) to 9% K<sup>-1</sup> (ref. 66)) far exceed the current range of  $\eta$ .

The pattern effects on  $\eta$  also have implications for regional and extreme rainfall variabilities, which are of particular interest to social development and policy making. Changes in  $\eta$  can be used to diagnose the changes in general circulation and water vapour lifetime, which are directly relevant to regional rainfall and extreme events<sup>24</sup>.  $\eta$  over land is generally lower than the global mean due to limited availability of water vapour<sup>67</sup>, thus making it strongly reliant on moisture transport and susceptible to SST warming patterns<sup>14,20</sup>. In addition, the evolving patterns of warming can drive different land–sea contrast responses<sup>14,68</sup> which can strongly influence regional  $\eta$  and extreme rainfall events<sup>69</sup>. Therefore, we hope our work could motivate further efforts on studying the changes in extreme rainfall events driven by the pattern effect.

## Online content

Any methods, additional references, Nature Portfolio reporting summaries, source data, extended data, supplementary information, acknowledgements, peer review information; details of author contributions and competing interests; and statements of data and code availability are available at <https://doi.org/10.1038/s41558-023-01678-5>.

## References

- Myhre, G. et al. PDRMIP: a precipitation driver and response model intercomparison project-protocol and preliminary results. *Bull. Am. Meteorol. Soc.* **98**, 1185–1198 (2017).
- DeAngelis, A. M., Qu, X., Zelinka, M. D. & Hall, A. An observational radiative constraint on hydrologic cycle intensification. *Nature* **528**, 249–253 (2015).
- Trenberth, K. Changes in precipitation with climate change. *Clim. Res.* **47**, 123–138 (2011).
- Allen, M. R. & Ingram, W. J. Constraints on future changes in climate and the hydrologic cycle. *Nature* **419**, 228–232 (2002).
- Muller, C. J. & O’Gorman, P. A. An energetic perspective on the regional response of precipitation to climate change. *Nat. Clim. Chang.* **1**, 266–271 (2011).
- Bala, G., Caldeira, K. & Nemani, R. Fast versus slow response in climate change: implications for the global hydrological cycle. *Clim. Dyn.* **35**, 423–434 (2010).
- Held, I. M. & Soden, B. J. Robust responses of the hydrological cycle to global warming. *J. Clim.* **19**, 5686–5699 (2006).
- Yang, F., Kumar, A., Schlesinger, M. E. & Wang, W. Intensity of hydrological cycles in warmer climates. *J. Clim.* **16**, 2419–2423 (2003).
- O’Gorman, P., Allan, R. P., Byrne, M. P. & Previdi, M. Energetic constraints on precipitation under climate change. *Surv. Geophys.* **33**, 585–608 (2012).

10. Samset, B. H. et al. Fast and slow precipitation responses to individual climate forcings: a PDRMIP multimodel study. *Geophys. Res. Lett.* **43**, 2782–2791 (2016).
11. Jeevanjee, N. & Romps, D. M. Mean precipitation change from a deepening troposphere. *Proc. Natl Acad. Sci. USA* **115**, 11465–11470 (2018).
12. Fläschner, D., Mauritsen, T. & Stevens, B. Understanding the intermodel spread in global-mean hydrological sensitivity. *J. Clim.* **29**, 801–817 (2016).
13. Vecchi, G. A. & Soden, B. J. Global warming and the weakening of the tropical circulation. *J. Clim.* **20**, 4316–4340 (2007).
14. Ma, J. et al. Responses of the tropical atmospheric circulation to climate change and connection to the hydrological cycle. *Annu. Rev. Earth Planet. Sci.* **46**, 549–580 (2018).
15. Hodnebrog, Ø. et al. Water vapour adjustments and responses differ between climate drivers. *Atmos. Chem. Phys.* **19**, 12887–12899 (2019).
16. Chou, C., Chen, C. A., Tan, P. H. & Chen, K. T. Mechanisms for global warming impacts on precipitation frequency and intensity. *J. Clim.* **25**, 3291–3306 (2012).
17. Myhre, G. et al. Frequency of extreme precipitation increases extensively with event rareness under global warming. *Sci. Rep.* **9**, 16063 (2019).
18. Barsugli, J. J. & Sardeshmukh, P. D. Global atmospheric sensitivity to tropical SST anomalies throughout the Indo-Pacific basin. *J. Clim.* **15**, 3427–3442 (2002).
19. Palmer, T. N. & Mansfield, D. A. Response of two atmospheric general circulation models to sea-surface temperature anomalies in the tropical East and West Pacific. *Nature* **310**, 483–485 (1984).
20. Bony, S. et al. Robust direct effect of carbon dioxide on tropical circulation and regional precipitation. *Nat. Geosci.* **6**, 447–451 (2013).
21. Xie, S.-P. et al. Global warming pattern formation: sea surface temperature and rainfall. *J. Clim.* **23**, 966–986 (2010).
22. Zhou, C., Lu, J., Hu, Y. & Zelinka, M. D. Responses of the Hadley circulation to regional sea surface temperature changes. *J. Clim.* **33**, 429–441 (2020).
23. Ma, J. & Xie, S.-P. Regional patterns of sea surface temperature change: a source of uncertainty in future projections of precipitation and atmospheric circulation. *J. Clim.* **26**, 2482–2501 (2013).
24. Sillmann, J. et al. Extreme wet and dry conditions affected differently by greenhouse gases and aerosols. *npj Clim. Atmos. Sci.* **2**, 24 (2019).
25. Allan, R. P. et al. Advances in understanding large-scale responses of the water cycle to climate change. *Ann. N. Y. Acad. Sci.* **1472**, 49–75 (2020).
26. Kvalevåg, M. M., Samset, B. H. & Myhre, G. Hydrological sensitivity to greenhouse gases and aerosols in a global climate model. *Geophys. Res. Lett.* **40**, 1432–1438 (2013).
27. Trenberth, K. E., Fasullo, J. T. & Kiehl, J. Earth's global energy budget. *Bull. Am. Meteorol. Soc.* **90**, 311–324 (2009).
28. Zhou, C., Zelinka, M. D. & Klein, S. A. Impact of decadal cloud variations on the Earth's energy budget. *Nat. Geosci.* **9**, 871–874 (2016).
29. Ceppi, P. & Gregory, J. M. Relationship of tropospheric stability to climate sensitivity and Earth's observed radiation budget. *Proc. Natl Acad. Sci. USA* **114**, 13126–13131 (2017).
30. Dong, Y., Proistosescu, C., Armour, K. C. & Battisti, D. S. Attributing historical and future evolution of radiative feedbacks to regional warming patterns using a Green's function approach: the preeminence of the Western Pacific. *J. Clim.* **32**, 5471–5491 (2019).
31. Andrews, T., Gregory, J. M. & Webb, M. J. The dependence of radiative forcing and feedback on evolving patterns of surface temperature change in climate models. *J. Clim.* **28**, 1630–1648 (2015).
32. Xie, S.-P., Kosaka, Y. & Okumura, Y. M. Distinct energy budgets for anthropogenic and natural changes during global warming hiatus. *Nat. Geosci.* **9**, 29–33 (2016).
33. Zhang, S., Stier, P. & Watson-Parris, D. On the contribution of fast and slow responses to precipitation changes caused by aerosol perturbations. *Atmos. Chem. Phys.* **21**, 10179–10197 (2021).
34. Watanabe, M. et al. Contribution of natural decadal variability to global warming acceleration and hiatus. *Nat. Clim. Chang.* **4**, 893–897 (2014).
35. Kosaka, Y. & Xie, S. P. Recent global-warming hiatus tied to equatorial Pacific surface cooling. *Nature* **501**, 403–407 (2013).
36. Zhou, C., Zelinka, M. D., Dessler, A. E. & Wang, M. Greater committed warming after accounting for the pattern effect. *Nat. Clim. Chang.* **11**, 132–136 (2021).
37. Neale, R. B. et al. *Description of the NCAR Community Atmosphere Model (CAM 5.0)*. NCAR Technical Notes. (NCAR, 2012).
38. Zhou, C., Zelinka, M. D. & Klein, S. A. Analyzing the dependence of global cloud feedback on the spatial pattern of sea surface temperature change with a Green's function approach. *J. Adv. Model. Earth Syst.* **9**, 2174–2189 (2017).
39. Thorpe, L. & Andrews, T. The physical drivers of historical and 21st century global precipitation changes. *Environ. Res. Lett.* **9**, 064024 (2014).
40. Pendergrass, A. G. The global-mean precipitation response to CO<sub>2</sub>-induced warming in CMIP6 models. *Geophys. Res. Lett.* **47**, e2020GL089964 (2020).
41. Trenberth, K. E., Dai, A., Rasmussen, R. M. & Parsons, D. B. The changing character of precipitation. *Bull. Am. Meteorol. Soc.* **84**, 1205–1217 (2003).
42. O'Gorman, P. A. & Muller, C. J. How closely do changes in surface and column water vapor follow Clausius–Clapeyron scaling in climate change simulations? *Environ. Res. Lett.* **5**, 025207 (2010).
43. Ming, Y., Ramaswamy, V. & Persad, G. Two opposing effects of absorbing aerosols on global-mean precipitation. *Geophys. Res. Lett.* **37**, 1–4 (2010).
44. Back, L. E. & Bretherton, C. S. Geographic variability in the export of moist static energy and vertical motion profiles in the tropical Pacific. *Geophys. Res. Lett.* **33**, L17810 (2006).
45. Williams, A. I. L., Stier, P., Dagan, G. & Watson-Parris, D. Strong control of effective radiative forcing by the spatial pattern of absorbing aerosol. *Nat. Clim. Chang.* **12**, 735–742 (2022).
46. Dagan, G. & Stier, P. Constraint on precipitation response to climate change by combination of atmospheric energy and water budgets. *npj Clim. Atmos. Sci.* **3**, 34 (2020).
47. Voigt, A. et al. Clouds, radiation, and atmospheric circulation in the present-day climate and under climate change. *WIREs Clim. Chang.* **12**, 1–22 (2021).
48. Eyring, V. et al. Overview of the Coupled Model Intercomparison Project Phase 6 (CMIP6) experimental design and organization. *Geosci. Model Dev.* **9**, 1937–1958 (2016).
49. Andrews, T., Gregory, J. M., Webb, M. J. & Taylor, K. E. Forcing, feedbacks and climate sensitivity in CMIP5 coupled atmosphere–ocean climate models. *Geophys. Res. Lett.* **39**, 1–7 (2012).
50. Watanabe, M., Kamae, Y., Shiogama, H., DeAngelis, A. M. & Suzuki, K. Low clouds link equilibrium climate sensitivity to hydrological sensitivity. *Nat. Clim. Chang.* **8**, 901–906 (2018).
51. He, J., Soden, B. J. & Kirtman, B. The robustness of the atmospheric circulation and precipitation response to future anthropogenic surface warming. *Geophys. Res. Lett.* **41**, 2614–2622 (2014).
52. Liu, C., Allan, R. P. & Huffman, G. J. Co-variation of temperature and precipitation in CMIP5 models and satellite observations. *Geophys. Res. Lett.* **39**, L13803 (2012).



53. Brohan, P., Kennedy, J. J., Harris, I., Tett, S. F. B. & Jones, P. D. Uncertainty estimates in regional and global observed temperature changes: a new data set from 1850. *J. Geophys. Res.* **111**, D12106 (2006).
54. Morice, C. P. et al. An updated assessment of near-surface temperature change from 1850: the HadCRUT5 data set. *J. Geophys. Res. Atmos.* **126**, e2019JD032361 (2021).
55. Lu, J., Chen, G. & Frierson, D. M. W. Response of the zonal mean atmospheric circulation to El Niño versus global warming. *J. Clim.* **21**, 5835–5851 (2008).
56. Rollings, M. & Merlis, T. M. The observed relationship between Pacific SST variability and Hadley cell extent trends in reanalyses. *J. Clim.* **34**, 2511–2527 (2021).
57. Allan, R. P., Willett, K. M., John, V. O. & Trent, T. Global changes in water vapor 1979–2020. *J. Geophys. Res. Atmos.* **127**, 1–23 (2022).
58. Frieler, K., Meinshausen, M., Schneider Von Deimling, T., Andrews, T. & Forster, P. Changes in global-mean precipitation in response to warming, greenhouse gas forcing and black carbon. *Geophys. Res. Lett.* **38**, 1–5 (2011).
59. Dai, A. Precipitation characteristics in eighteen coupled climate models. *J. Clim.* **19**, 4605–4630 (2006).
60. Ma, S. & Zhou, T. Robust strengthening and westward shift of the tropical Pacific Walker circulation during 1979–2012: a comparison of 7 sets of reanalysis data and 26 CMIP5 models. *J. Clim.* **29**, 3097–3118 (2016).
61. Gregory, J. M. & Andrews, T. Variation in climate sensitivity and feedback parameters during the historical period. *Geophys. Res. Lett.* **43**, 3911–3920 (2016).
62. Armour, K. C., Marshall, J., Scott, J. R., Donohoe, A. & Newsom, E. R. Southern Ocean warming delayed by circumpolar upwelling and equatorward transport. *Nat. Geosci.* **9**, 549–554 (2016).
63. Heede, U. K. & Fedorov, A. V. Eastern equatorial Pacific warming delayed by aerosols and thermostat response to CO<sub>2</sub> increase. *Nat. Clim. Chang.* **11**, 696–703 (2021).
64. Seager, R. et al. Strengthening tropical Pacific zonal sea surface temperature gradient consistent with rising greenhouse gases. *Nat. Clim. Chang.* **9**, 517–522 (2019).
65. Stephens, G. L. et al. Regional intensification of the tropical hydrological cycle during ENSO. *Geophys. Res. Lett.* **45**, 4361–4370 (2018).
66. Adler, R. F., Gu, G., Sapiano, M., Wang, J.-J. & Huffman, G. J. Global precipitation: means, variations and trends during the satellite era (1979–2014). *Surv. Geophys.* **38**, 679–699 (2017).
67. Gimeno, L. et al. Oceanic and terrestrial sources of continental precipitation. *Rev. Geophys.* **50**, RG4003 (2012).
68. He, J. & Soden, B. J. Anthropogenic weakening of the tropical circulation: the relative roles of direct CO<sub>2</sub> forcing and sea surface temperature change. *J. Clim.* **28**, 8728–8742 (2015).
69. Taylor, C. M. et al. Frequency of extreme Sahelian storms tripled since 1982 in satellite observations. *Nature* **544**, 475–478 (2017).

**Publisher's note** Springer Nature remains neutral with regard to jurisdictional claims in published maps and institutional affiliations.

**Open Access** This article is licensed under a Creative Commons Attribution 4.0 International License, which permits use, sharing, adaptation, distribution and reproduction in any medium or format, as long as you give appropriate credit to the original author(s) and the source, provide a link to the Creative Commons license, and indicate if changes were made. The images or other third party material in this article are included in the article's Creative Commons license, unless indicated otherwise in a credit line to the material. If material is not included in the article's Creative Commons license and your intended use is not permitted by statutory regulation or exceeds the permitted use, you will need to obtain permission directly from the copyright holder. To view a copy of this license, visit <http://creativecommons.org/licenses/by/4.0/>.

© The Author(s) 2023, corrected publication 2023

## Methods

### SST warming patch experiments

The SST warming patch experiments are based on the Community Atmospheric Model 5.3 (ref. 37) in the Community Earth System Model 1.2.1, with a resolution of 1.9° latitude x 2.5° longitude and 30 vertical levels. A baseline run is conducted with monthly SST, sea ice and external forcing fixed at the level of the year 2000. Next, 80 simulations are conducted with a warming patch individually applied on the prescribed SST in the baseline run. Each SST anomaly patch  $p$  ( $p = 1, \dots, 80$ ) takes the form of a cosine hump<sup>18,38</sup>:

$$\Delta\text{SST}_p(\text{lat}, \text{lon}) = A \cos^2\left(\frac{\pi}{2} \frac{\text{lat} - \text{lat}_p}{\text{lat}_w}\right) \cos^2\left(\frac{\pi}{2} \frac{\text{lon} - \text{lon}_p}{\text{lon}_w}\right), \quad (4)$$

with a maximum of 4 K ( $A = 4$  K) warming at the patch centre ( $\text{lat}_p, \text{lon}_p$ ) and a radius of 10° latitude ( $\text{lat}_w = 10^\circ$ ) and 40° longitude ( $\text{lon}_w = 40^\circ$ ), where  $|\text{lat} - \text{lat}_p| \leq \text{lat}_w$  and  $|\text{lon} - \text{lon}_p| \leq \text{lon}_w$ . Figure 1a shows the geographical location of the centre of all SST warming patches. Another set of 80 simulations are conducted similarly to the warming patch experiments but replacing the warming patches with cooling patches of the same magnitude ( $A = -4$  K). More details of the experimental set-up can be found in ref. 38. All the simulations are run for 40 years, and the average of the past 30 years is used to avoid spin-up effects in the first months or years.

It should be noted that the land surface temperature is still allowed to adjust in the model, despite fixing SSTs. Thus, there are some land surface temperature responses to the SST anomaly patch that could lead to a spread of changes in global-mean surface temperature among the experiments.

### Hydrological sensitivity

The hydrological sensitivity ( $\eta$ ) parameter quantifies the sensitivity of temperature-mediated global-mean precipitation responses to an increase in global-mean surface temperature<sup>4,7,12,70-72</sup>. For SST patch experiments in this work, as the only changes in our patch experiments are from SST ('SST warming patch experiments'), fast adjustments are therefore not considered, and the changes in precipitation are only SST-mediated responses (that is, slow responses). We therefore directly derive  $\eta$  for SST patch experiments as follows:

$$\eta = \frac{\Delta P/P_0}{\Delta T}, \quad (5)$$

where  $P_0$  denotes the baseline precipitation rate and  $\Delta P$  refers to the changes in global-mean precipitation, so that the numerator indicates the relative change in precipitation.  $\Delta T$  is the global-mean near-surface temperature change. To avoid division by small responses of global-mean near-surface temperature, which could lead to unrealistically large  $\eta$ , we calculate the changes in global-mean temperature between the warming patch experiment and corresponding cooling patch experiment following ref. 38. Only cases that showed significantly different ( $P$  values below 0.01 according to a  $t$ -test using 30 years annual-mean output) global-mean surface temperature are used (77 out of 80 experiments).

Another way to derive  $\eta$  is to calculate the slope of a Gregory-style regression<sup>73</sup> between global-mean precipitation and surface temperature changes<sup>2,26,72</sup>. It is also helpful to separate the adjustment and temperature-mediated responses to climate forcings such as greenhouse gases and anthropogenic aerosols<sup>12</sup>. We use the Gregory-style approach to derive  $\eta$  from fully coupled CMIP5 models<sup>74</sup>. Following the method from ref. 2, we use 150 years (except for IPSL-CM5A-MR which has only 140 years data available) annual averages of precipitation and near-surface air temperature from the pre-industrial control (piControl) and abrupt4xCO<sub>2</sub> experiments. For each year in the abrupt4xCO<sub>2</sub> run, the response

of precipitation and temperature is calculated as the difference relative to the same year in the 21 year smoothed piControl run, which allows to reduce the possible impacts from climate model drift. The hydrological sensitivity is then calculated as the slope between global-mean precipitation and near-surface temperature, whereas the  $y$ -intercept denotes the rapid adjustment. The good regressions show the reliability of  $\eta$  derived from this method (Supplementary Fig. 17).

### Energetic decompositions

The latent heat released from global-mean precipitation is balanced by ARC and downward surface sensible flux ( $-\text{SH}$ ), which is widely used as an energetic constraint to study global precipitation responses<sup>5,33</sup>.

$$L\Delta P = \Delta\text{ARC} - \Delta\text{SH}, \quad (6)$$

where  $L$  denotes the latent heat of condensation and ARC refers to the ARC, which is the difference of longwave (LW) and shortwave (SW) fluxes between the top of the atmosphere (TOA) and the surface (SUR):

$$\text{ARC} = (\text{LW}_{\text{TOA}} + \text{SW}_{\text{TOA}}) - (\text{LW}_{\text{SUR}} + \text{SW}_{\text{SUR}}), \quad (7)$$

where all the radiative fluxes are defined as positive downward.

We can therefore decompose the hydrological sensitivity into constraints from ARC

$$\eta_{\text{ARC}} = \frac{\Delta\text{ARC}/LP_0}{\Delta T}, \quad (8)$$

and contributions from sensible heat flux by replacing ARC with SH:

$$\eta_{\text{SH}} = \frac{\Delta(-\text{SH})/LP_0}{\Delta T}. \quad (9)$$

Using a radiative call to calculate the radiative fluxes at TOA and surface, we are able to further derive the contributions from clouds ( $\text{ARC}_{\text{cloud}}$ ) and clear sky ( $\text{ARC}_{\text{clearsky}}$ ):

$$\text{ARC} = \text{ARC}_{\text{cloud}} + \text{ARC}_{\text{clearsky}}. \quad (10)$$

This decomposition enables us to distinguish energetic constraints arising from clouds or clear sky, by replacing ARC with  $\text{ARC}_{\text{cloud}}$  or  $\text{ARC}_{\text{clearsky}}$ .

### Green's function approach

We make use of the Green's function approach to examine the local contributions to global precipitation changes. The change of a global-mean variable can be interpreted as the sum of a linear contribution from each grid box  $i$  and an error term, in a discrete form of Green's function following ref. 38:

$$\Delta y = \sum_i \frac{\partial y}{\partial \text{SST}_i} \Delta \text{SST}_i + \varepsilon, \quad (11)$$

where  $y$  denotes any global-mean variables of interest,  $\text{SST}_i$  refers to the SST in a grid box  $i$ , and  $\varepsilon$  denotes an error term that contains all the nonlinear components<sup>18,30</sup>. The grid-wise sensitivity of  $y$  to  $\text{SST}_i$  (that is,  $\partial y/\partial \text{SST}_i$ ) is the weighted sum of the patch-wise sensitivity of  $y$  to  $\text{SST}_p$  of the patches which cover the grid  $i$ :

$$\frac{\partial y}{\partial \text{SST}_i} = \frac{\sum_p \Delta \text{SST}_p \frac{y_w - y_c}{\text{SST}_{p,w} - \text{SST}_{p,c}} \frac{S_i}{S_p}}{\sum_p \Delta \text{SST}_p} \quad (12)$$

where the subscript  $w$  in  $\text{SST}_{p,w}$  denotes a warming SST patch, the subscript  $c$  in  $\text{SST}_{p,c}$  denotes the conjugating cooling patch, and  $S_i$  and  $S_p$  refer to the area of the specific grid box  $i$  and patch  $p$ , respectively.

### The spread of the pattern effect in CMIP5 models

Here we illustrate how the normalized distribution of the two terms in equation (3) are derived. We take advantage of Green's function derived from CAM5 SST patch experiments to reproduce the global-mean precipitation changes for the CMIP5 models by inputting their spatial SST warming patterns only. For example, for model  $k$ , which is a GCM with a patterned SST warming, the reconstructed precipitation change is

$$\Delta P_{k,\text{greens}} = \sum_i \left( \frac{\partial P}{\partial \text{SST}_i} \right)_{\text{CAM5}} \Delta \text{SST}_i, \quad (13)$$

where  $\left( \frac{\partial P}{\partial \text{SST}_i} \right)_{\text{CAM5}}$  is the Green's function derived from CAM5 for each grid box (equation (12)). The differences in the Green's function approach reconstructed precipitation changes therefore account for the different warming pattern effect, given the spatial SST warming pattern within each model is the only input (and only difference). It is noteworthy that we do not expect this CAM5 Green's function approach reconstructed precipitation to perfectly reproduce another model's estimated precipitation, due to model differences, other physical processes that impact on precipitation yet are not associated with SST changes, and nonlinear contributions (equation 11). However, the reconstructed precipitation changes are found to predict the model-estimated precipitation responses in the 24 CMIP5 models reasonably well, with robust correlations (Supplementary Fig. 18), although the relationships do not follow the 1:1 ratio and vary from model to model (Supplementary Fig. 19), as follows:

$$\Delta P_k = \frac{\partial P_k}{\partial P_{\text{greens}}} \times \Delta P_{k,\text{greens}} = \alpha_k \times \Delta P_{k,\text{greens}} \quad (14)$$

$$\eta_k = \alpha_k \times \frac{\partial P_{k,\text{greens}}}{\partial T} = \alpha_k \times \left( \sum_i \left( \frac{\partial P}{\partial \text{SST}_i} \right)_{\text{CAM5}} \times \frac{\partial \text{SST}_i}{\partial T} \right). \quad (15)$$

The variation of the ratios ( $\alpha$ ) between the model-estimated and Green's function reconstructed precipitation changes among models is caused by model differences excluding the warming pattern and can be used to derive the spread of the atmospheric model term. On the other side, the differences in Green's function approach reconstructed precipitation changes account for the different warming pattern effect, as the patterned SST warming is the only input. Therefore, we can use the regression slope between the model-estimated and reconstructed precipitation changes as a factor representing model differences ( $\alpha$ ), which accounts for models differences other than the warming pattern, and the spread of Green's function approach reconstructed precipitation in the 24 CMIP5 models to account for the pattern effect.

The weak relationship between the atmospheric model term and pattern effect term (Supplementary Fig. 18) indicates that both independently contribute to the estimated  $\eta$ . It is noteworthy that, unlike radiative forcing, for which the uncertainties can be linearly added from each independent climate agents<sup>75</sup>, the reconstructed  $\eta$  is obtained by multiplying the two terms as they are chain processes<sup>76</sup>. Therefore, the spread of  $\eta$  is nonlinearly contributed by the averages and deviations of the two terms simultaneously.

As the atmospheric difference term and the pattern difference term are uncorrelated (Supplementary Fig. 18), the variance of reconstructed  $\eta$  among GCMs is as follows:

$$\text{Var}(XY) = \sigma_X^2 \sigma_Y^2 + \sigma_X^2 \bar{\mu}_Y^2 + \bar{\mu}_X^2 \sigma_Y^2 \quad (16)$$

where  $X$  refers to the atmospheric model difference term, and  $Y$  refers to the warming pattern difference term in this work.  $\sigma$  denotes the standard deviation, and  $\bar{\mu}$  denotes the average. The variance of  $\eta$  in CMIP models should be

$$\text{Var}(XY)_C = \sigma_{X,C}^2 \sigma_{Y,C}^2 + \sigma_{X,C}^2 \bar{\mu}_{Y,C}^2 + \bar{\mu}_{X,C}^2 \sigma_{Y,C}^2 \quad (17)$$

where the subscript C denotes average and standard deviation estimated from CMIP models. For AMIP models,  $\sigma_Y = 0$  as the SST pattern is the same. Then the variance of  $\eta$  in AMIP models should be

$$\text{Var}(XY)_A = \sigma_{X,A}^2 \bar{\mu}_{Y,A}^2 \quad (18)$$

where the subscript A denotes variables estimated from AMIP models.  $\bar{\mu}_{Y,A}$  is larger in amip4K and amipFuture experiments than  $\bar{\mu}_{Y,C}$  from the fully coupled CMIP5 about4xCO<sub>2</sub> experiment, based on the SST pattern quantified by the Green's function approach (vertical lines in Fig. 4b). Therefore,  $\text{Var}(XY)_C$  does not necessarily need to be larger than  $\text{Var}(XY)_A$ . Taking the values of the average and standard deviation into equations (17) and (18), we obtain almost the same spread of  $\eta$  in CMIP and AMIP models.

### Reconstruct historical global-mean precipitation

The changes in global-mean precipitation are modulated by the sum of a fast component (the changes in atmospheric absorption ( $\Delta AA$ ) directly induced by aerosols and greenhouse gases through atmospheric-only processes, independent of surface temperature changes)<sup>9,43,77</sup>, a slow component ( $\eta \Delta T$ , scaled with global-mean temperature changes)<sup>4,9,10,39,77</sup> and contribution from the surface sensible heat ( $\Delta SH$ )<sup>78</sup>, as in equation (19),

$$\Delta P = \eta \Delta T \times P_0 - (\Delta AA + \Delta SH)/L, \quad (19)$$

where  $L$  denotes the latent heat of condensation so all terms are in units of mm d<sup>-1</sup>. Conventionally, the slow component is derived from the hydrological sensitivity parameter  $\eta$  multiplied by global-mean temperature changes<sup>39,77</sup>. Here we set  $\eta$  to 2.3% K<sup>-1</sup>, which is the ensemble mean from 24 CMIP5 models. However, this framework does not consider the pattern effect, which modulates the precipitation changes through the slow component as well. Therefore, we put forward a framework to account for the pattern effect,

$$\Delta P = \sum_i \left( \frac{\partial P}{\partial \text{SST}_i} \right) \Delta \text{SST}_i - (\Delta AA + \Delta SH)/L, \quad (20)$$

where  $\left( \frac{\partial P}{\partial \text{SST}_i} \right)$  is the Green's function derived from CAM5 for each grid box and  $\text{SST}_i$  refers to the SST in a grid box  $i$ .  $\Delta AA$  and  $\Delta SH$  are derived from the ensemble-mean CMIP6 historical and SSP1-2.6 simulations. Specifically,  $\Delta AA$  is calculated as the sum of instantaneous TOA radiative forcing from each climate agent multiplied by its corresponding scaling factor, following the methods from ref. 79 and ref. 77. The fast components ( $\Delta AA$  and  $\Delta SH$ ) are kept the same for both approaches, so the differences are only caused by the pattern effect.

Although the Green's function approach used here is derived from only one model (CAM5) and neglects nonlinear contributions as well as impacts from changes in land temperature, our framework can still reasonably reproduce the observed precipitation. Nevertheless, future studies are suggested to compare the Green's function derived from different GCMs to understand its model dependency.

### CMIP models

The 24 CMIP5 models used in this study to investigate the inter-model spread of  $\eta$  are documented in Supplementary Table 1. Sea ice, ocean, land and atmosphere are fully coupled for the piControl and abrupt4xCO<sub>2</sub> experiments. We use monthly output from one ensemble member (r1i1p1) in the CMIP5 models. In addition to the fully coupled simulations, we also use the atmosphere-only experiments from the

Atmospheric Models Intercomparison Project (AMIP)<sup>74,80</sup>. SST is prescribed to present-day values in the standard amip experiment. The SST is uniformly increased by 4 K in the amip4K experiment compared with the amip. The increased warming is patterned in the amipFuture experiment while keeping the global-mean SST increased still to 4 K.

For historical precipitation analysis shown in Fig. 5, this work uses 11 CMIP6 models (Supplementary Table 2), including the fully coupled CMIP6 historical simulations and the amip-hist simulations. Both sets of simulations use the same external forcing fields. Sea ice, ocean, land and atmosphere are coupled in CMIP6 historical simulations (from 1850 to 2020), while sea ice and ocean are prescribed from observations in AMIP6 simulations (from 1980 to 2014)<sup>48</sup>.

### Observational and reanalysis datasets

We incorporate several observational and reanalysis data sets to conduct our analysis. Specifically, observed SST data from 1980 to 2020 are obtained from two sources: the HadCRUT observed gridded SST data<sup>54</sup> from Met office Hadley Centre and the NOAA monthly reconstructed SST data<sup>81</sup>. In addition, we use the precipitation and SST data sets over the same period (1980 to 2020) from ERA5 atmospheric reanalysis data<sup>82</sup>. We also utilize observational precipitation data from 1979 to 2020 from the GPCP observational dataset<sup>83</sup>, which is derived from rain gauge stations, ground sounding and satellite observations.

### Data availability

CMIP5 and CMIP6 model data sets used in this study are publicly available at CMIP5 (<https://esgf-node.llnl.gov/search/cmip5/>) and CMIP6 (<https://esgf-node.llnl.gov/search/cmip6/>). The HadCRUT observed gridded sea surface temperature data at a resolution of 5°, covering from January 1850 to present day, can be found at <https://www.metoffice.gov.uk/hadobs/hadcrut5/data/current/download.html>. The NOAA SST data sets cover the period from 1854 to present day at a resolution of 2° and are available at <https://psl.noaa.gov/data/gridded/data.noaa.ersst.v5.html>. The ERA5 reanalysis data sets cover the period from 1950 to present with a resolution of approximately 30 km, which can be accessed at <https://www.ecmwf.int/en/forecasts/dataset/ecmwf-reanalysis-v5>. The Global Precipitation Climatology Project precipitation data sets, covering the period from 1979 to present day at a resolution of 2.5°, are available at <https://psl.noaa.gov/data/gridded/data.gpcp.html>. The data necessary to reproduce the results are available at <https://zenodo.org/record/7787504> (ref. 84).

### Code availability

The model codes of CESM1.2-CAM5.3 are publicly available at <http://www.cesm.ucar.edu/models/cesm1.2>. The codes for generating the figures in this work are available at <https://zenodo.org/record/7787504> (ref. 84).

### References

- Bala, G., Duffy, P. B. & Taylor, K. E. Impact of geoengineering schemes on the global hydrological cycle. *Proc. Natl Acad. Sci. USA* **105**, 7664–7669 (2008).
- Pendergrass, A. G. & Hartmann, D. L. Global-mean precipitation and black carbon in AR4 simulations. *Geophys. Res. Lett.* **39**, 1–6 (2012).
- Andrews, T., Forster, P. M. & Gregory, J. M. A surface energy perspective on climate change. *J. Clim.* **22**, 2557–2570 (2009).
- Gregory, J. & Webb, M. Tropospheric adjustment induces a cloud component in CO<sub>2</sub> forcing. *J. Clim.* **21**, 58–71 (2008).
- Taylor, K. E., Stouffer, R. J. & Meehl, G. A. An overview of CMIP5 and the experiment design. *Bull. Am. Meteorol. Soc.* **93**, 485–498 (2012).
- Bellouin, N. et al. Bounding global aerosol radiative forcing of climate change. *Rev. Geophys.* **58**, 1–45 (2020).
- Ghan, S. et al. Challenges in constraining anthropogenic aerosol effects on cloud radiative forcing using present-day spatiotemporal variability. *Proc. Natl Acad. Sci. USA* **113**, 5804–5811 (2016).
- Allan, R. P. et al. Physically consistent responses of the global atmospheric hydrological cycle in models and observations. *Surv. Geophys.* **35**, 533–552 (2014).
- Myhre, G. et al. Sensible heat has significantly affected the global hydrological cycle over the historical period. *Nat. Commun.* **9**, 1922 (2018).
- Andrews, T., Forster, P. M., Boucher, O., Bellouin, N. & Jones, A. Precipitation, radiative forcing and global temperature change. *Geophys. Res. Lett.* **37**, n/a–n/a (2010).
- Gates, W. L. et al. An overview of the results of the Atmospheric Model Intercomparison Project (AMIP I). *Bull. Am. Meteorol. Soc.* **80**, 29–55 (1999).
- Huang, B. et al. Extended Reconstructed Sea Surface Temperature, version 5 (ERSSTv5): upgrades, validations, and intercomparisons. *J. Clim.* **30**, 8179–8205 (2017).
- Hersbach, H. et al. The ERA5 global reanalysis. *Q. J. R. Meteorol. Soc.* **146**, 1999–2049 (2020).
- Adler, R. F. et al. The version-2 Global Precipitation Climatology Project (GPCP) monthly precipitation analysis (1979–present). *J. Hydrometeorol.* **4**, 1147–1167 (2003).
- Zhang, S., Stier, P., Dagan, G., Zhou, C. & Wang, M. Supporting data for ‘Sea surface warming patterns drive hydrological sensitivity uncertainties’. Zenodo <https://doi.org/10.5281/zenodo.7787504> (2023).

### Acknowledgements

S.Z., G.D. and P.S. are supported by the European Research Council (ERC) project constRaining the EffECts of Aerosols on Precipitation (RECAP) under the European Union’s Horizon 2020 research and innovation programme with grant agreement number 724602. S.Z. is supported by the Clarendon Scholarship from University of Oxford and the NERC-Oxford Doctorial Training Partnership in Environmental Research. P.S. acknowledges funding from the FORCES project under the European Union’s Horizon 2020 research program with grant agreement 821205. G.D. was also supported by the Israeli Science Foundation (grant number 1419/21). M.W. is supported by the Natural Science Foundation of China (41925023 and 91744208). C.Z.’s work was supported by the National Natural Science Foundation of China (NSFC 41875095 and 42075127), Research Funds for the Frontiers Science Center for Critical Earth Material Cycling, Nanjing University, and the Fundamental Research Funds for the Central Universities (0207/14380189). We acknowledge the WCRP’s Working Group on Coupled Modeling, which is responsible for CMIP, and we thank the climate modelling groups (listed in Supplementary Tables 1 and 2) for producing and making available their model output. GPCP Precipitation data were provided by the NOAA/OAR/ESRL PSL, Boulder, CO, USA, from their website at <https://psl.noaa.gov/data/gridded/data.gpcp.html>. We thank L. Wilcox and M. Allen for useful discussions.

### Author contributions

S.Z. initiated the study and performed the analysis. C.Z. contributed the CAM5 SST patch experiments. All authors discussed and interpreted the results. S.Z. prepared the paper with contributions from all co-authors.

### Competing interests

The authors declare no competing interests.

### Additional information

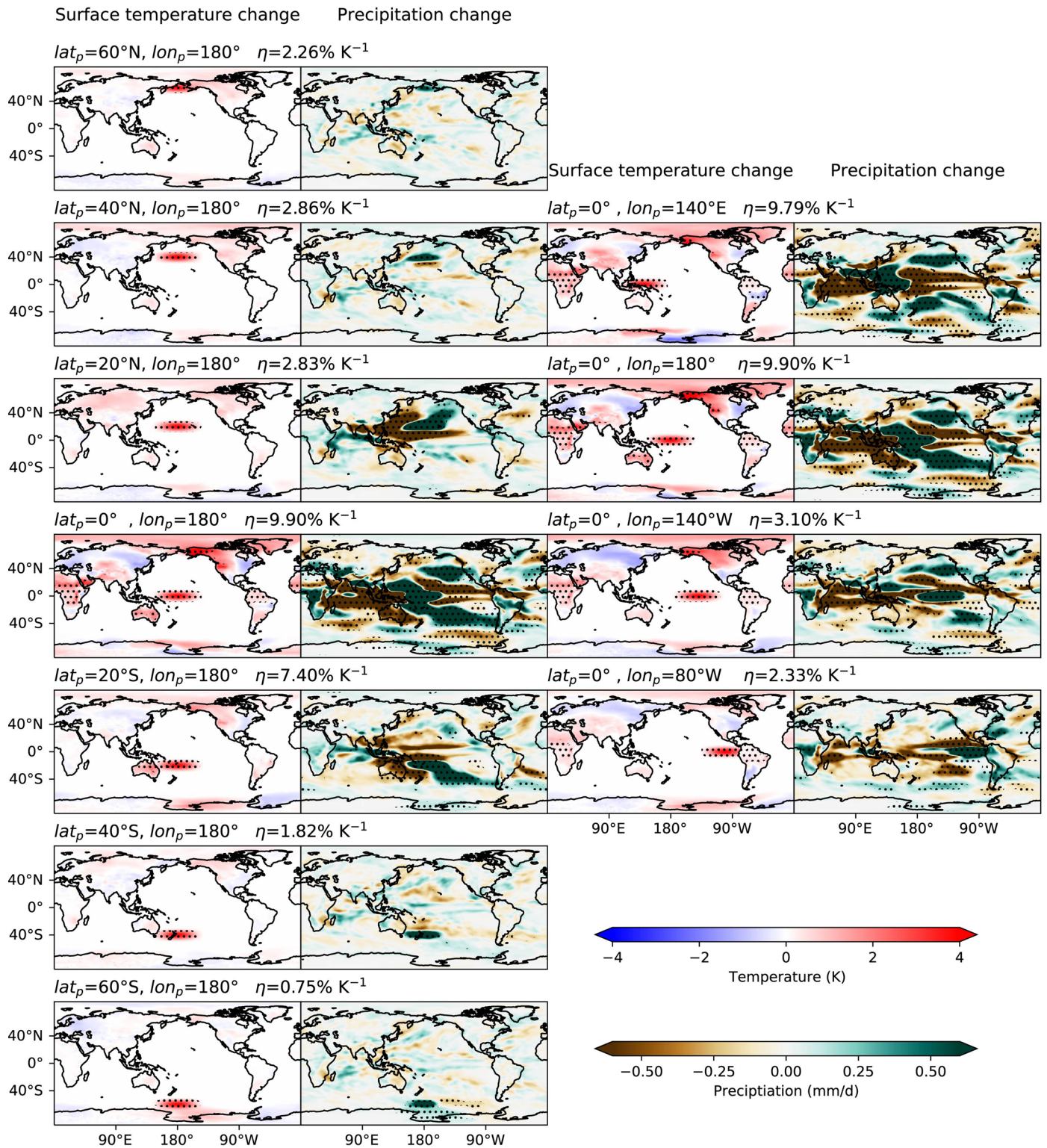
**Extended data** is available for this paper at <https://doi.org/10.1038/s41558-023-01678-5>.

**Supplementary information** The online version contains supplementary material available at <https://doi.org/10.1038/s41558-023-01678-5>.

**Correspondence and requests for materials** should be addressed to Shipeng Zhang.

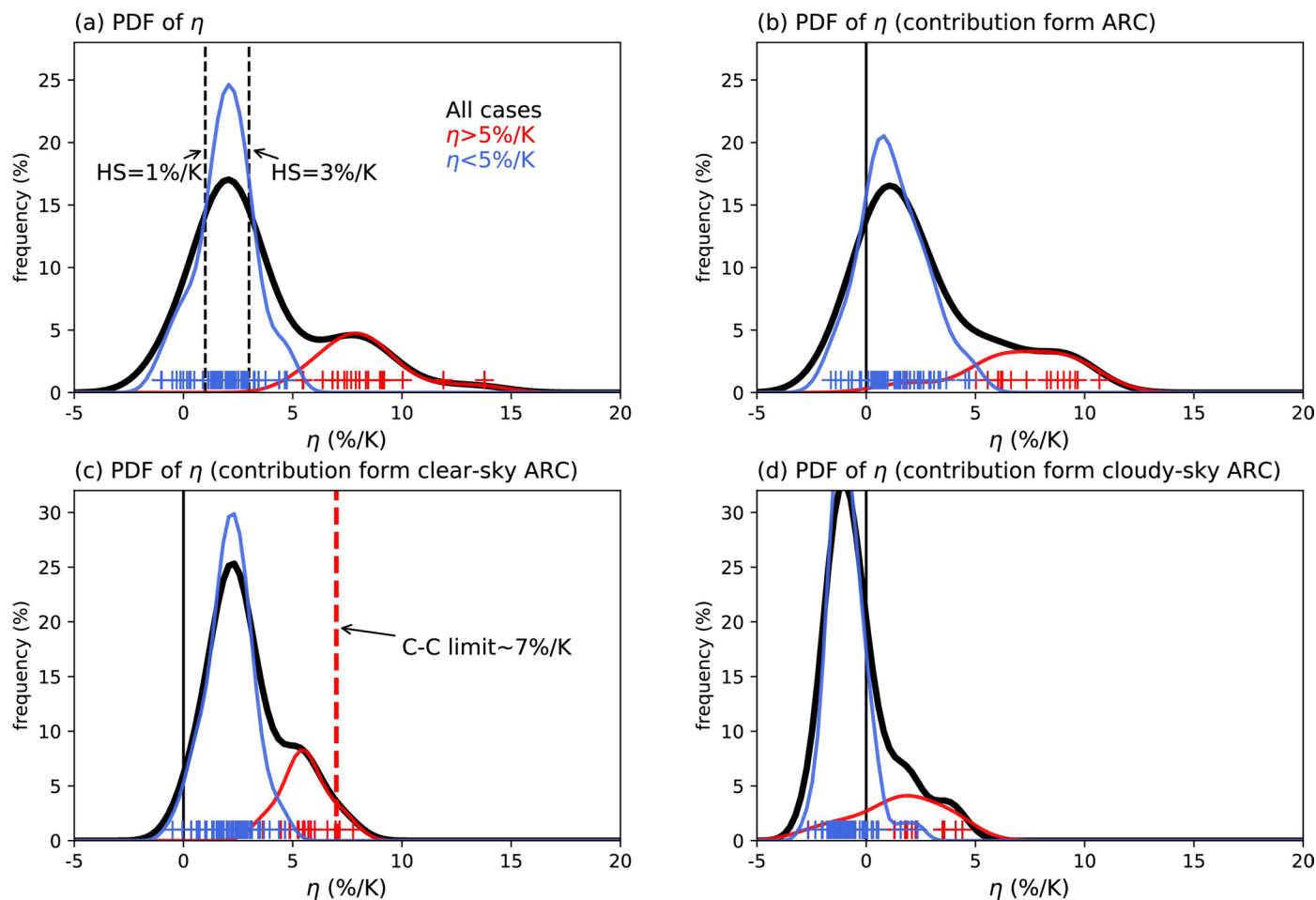
**Peer review information** *Nature Climate Change* thanks Richard Allan, Jian Ma and Masahiro Watanabe for their contribution to the peer review of this work.

**Reprints and permissions information** is available at [www.nature.com/reprints](http://www.nature.com/reprints).



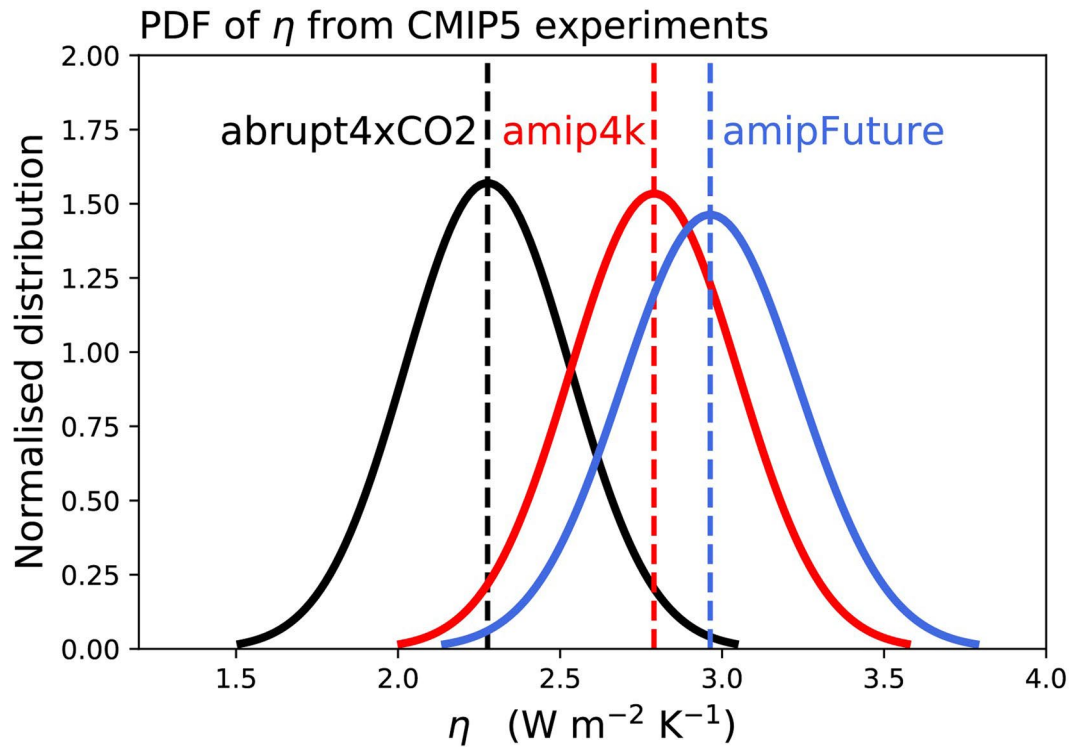
**Extended Data Fig. 1 | Geographical distribution of surface temperature and precipitation changes in CAM5 representative warming patch experiments.** The geographical distribution of surface temperature (first and third columns) and precipitation (second and fourth columns) changes between the representative warming patch experiments and baseline climatology from the CAM5 model. The two columns on the left show the changes in surface

temperature and precipitation as the centre of SST warming patch varies along the longitude 180 degree. The two columns on the right show the changes in surface temperature and precipitation as the centre of SST warming patch varies along the equator. Also shown are the patch center location and the hydrological sensitivity estimated from the corresponding experiment.



**Extended Data Fig. 2 | Probability distribution of hydrological sensitivity and its contributions from all-sky, clear-sky, and cloudy-sky atmospheric radiative cooling.** Estimated probability distribution of the (a) hydrological sensitivity ( $\eta$ ) (black line), (b)  $\eta$  caused by atmospheric radiative cooling (ARC), (c)  $\eta$  caused by atmospheric radiative cooling from clear sky, and (d)  $\eta$  caused by atmospheric radiative cooling from cloudy sky, derived from CAM5 patch

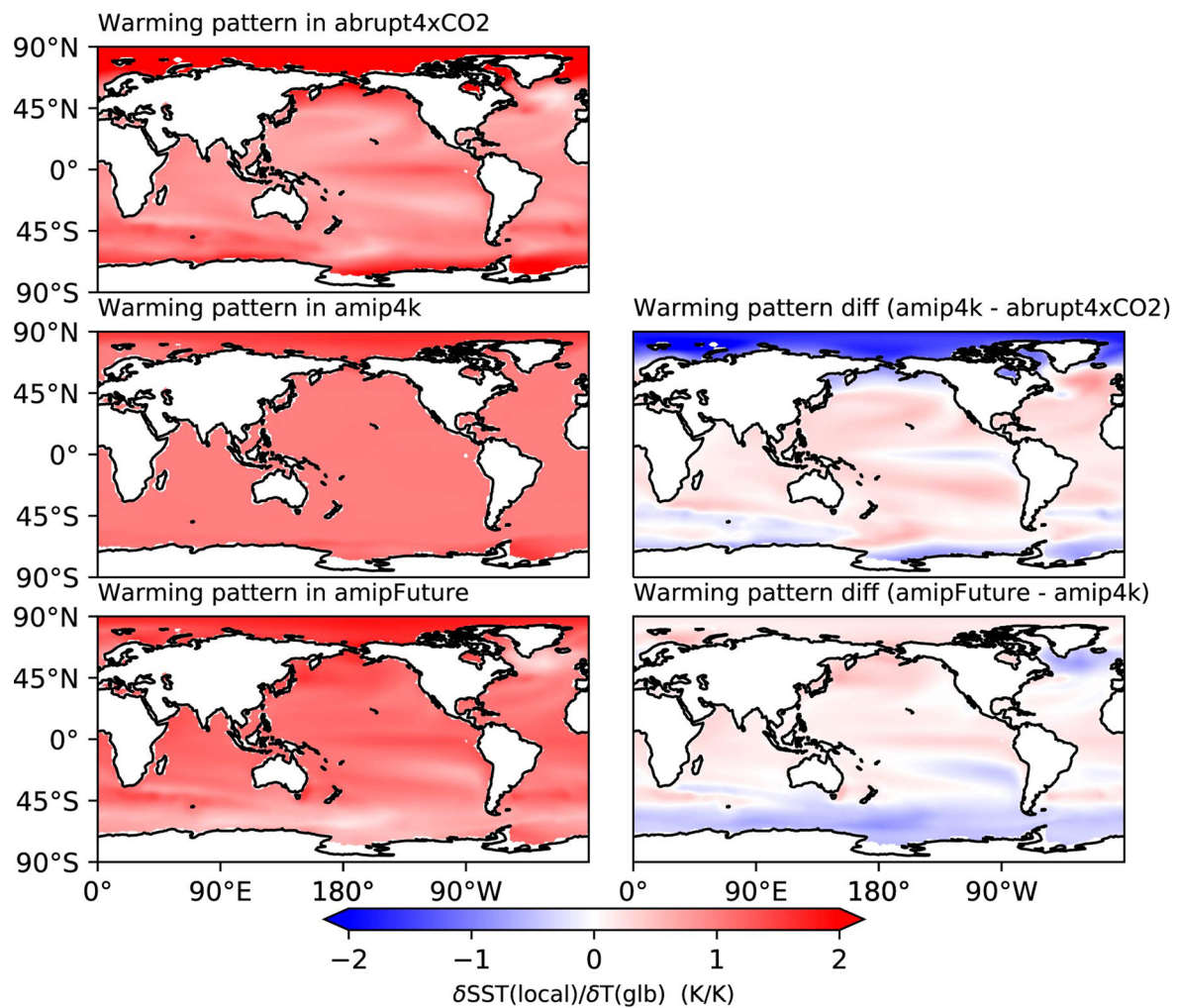
experiments (Methods). Red dashed line in (c) indicates the Clausius-Clapeyron relationship governed water vapour increase rate. Blue and red lines indicate the probability distribution (weighted by their ratio to total cases) derived from patch experiments with  $\eta$  smaller and larger than  $5\% K^{-1}$  respectively. Each plus sign indicates the value of  $\eta$  estimated from the corresponding patch experiment.



**Extended Data Fig. 3 | Estimated distribution of hydrological sensitivity from abrupt4xCO2, amip4k, and amipFuture experiments.** The estimated distribution of hydrological sensitivity ( $\eta$ ) estimated from abrupt4xCO2 (black

line), amip4k (red line), and amipFuture (blue line) experiments (models in Supplementary Table 1). The spread is shown as Gaussian curves given by the ensemble mean and standard deviation derived from the participating models.





**Extended Data Fig. 4 | Warming pattern for abrupt4xCO<sub>2</sub>, amip4K, and amipFuture experiments.** (left column) The ensemble-mean warming pattern from 24 models for abrupt4xCO<sub>2</sub> experiment, and the SST pattern in amip4K and amipFuture experiments. (right column) Also shown are the differences between them.